DFT STUDY OF $BaKN_3$ AND $BaRbN_3$ PEROVSKITES: REVEALING THEIR MECHANICAL, OPTOELECTRONIC, AND MAGNETIC PROPERTIES

ESTUDIO DFT DE PEROVSKITAS $BaKN_3$ Y $BaRbN_3$: REVELANDO SUS PROPIEDADES MECÁNICAS, OPTOELECTRÓNICAS Y MAGNÉTICAS

Saadiya Benatmane[a,b†], Samira Hezil-Ziane[a]

a) Faculty of Sciences and Technology, Department of Science and Technology, BP227 Abdelhamid Ibn Badis University, 27000, Mostaganem, Algeria; saadia.benotmane@univ-mosta.dz†
b) Laboratory of Modelling and Simulation of Materials Science, Djillali Liabès University of Sidi Bel-Abbès, 22000, Sidi Bel-Abbes, Algeria.
† corresponding author

Recibido 7/4/2024; Aceptado 9/11/2024

The full-potential linearized augmented plane waves (FP-LAPW) method, which is based entirely on density functional theory (DFT), was used to investigate the structural, electronic, magnetic, optical, and elastic properties of $BaXN_3$ (X=K, Rb). This method also employs the Perdew-Burke-Ernzerhof generalized gradient approximation (GGA-PBE) and a modified Beck Johnson TB-mBJ potential in the exchange correlation term. When the resulting structural properties were examined, the findings s howed that our compounds are more stable when they are configured as ferromagnetic materials. The total and partial density of state curves were used to assess the contributions of the various bands. Additionally, we discovered that the total magnetic moment is an integer of 6 μB, confirming the half-metallic nature. The mechanical stability of these compounds has been discovered. The elastic parameters are obtained, including the elastic constants, bulk modulus, anisotropy factor, Poisson's ratio, and Pugh's ratio.

El método de ondas planas aumentadas linealizadas de potencial total (FP-LAPW), que se basa completamente en la teoría funcional de la densidad (DFT), se utilizó para investigar las propiedades estructurales, electrónicas, magnéticas, ópticas y elásticas de $BaXN_3$ (X= K, Rb). Este método también emplea la aproximación de gradiente generalizado de Perdew-Burke-Ernzerhof (GGA-PBE) y un potencial TB-mBJ de Beck Johnson modificado en el término de correlación de intercambio. Cuando se examinaron las propiedades estructurales resultantes, los hallazgos mostraron que nuestros compuestos son más estables cuando están configurados como materiales ferromagnéticos. Se utilizaron curvas de densidad total y parcial de estados para evaluar las contribuciones de las distintas bandas. Además, descubrimos que el momento magnético total es un número entero de 6 μB, lo que confirma l a naturaleza semimetálica. Se ha descubierto la estabilidad mecánica de estos compuestos. Se obtienen los parámetros elásticos, incluidas las constantes elásticas, el módulo de volumen, el factor de anisotropía, el índice de Poisson y el índice de Pugh.

PACS: Density-functional theory atomic and molecular physics (Teoría del funcional de densidad física atómica y molecular), structural properties of materials (propiedades estructurales de los materiales), Perovskites (Perovskitas); Mechanical, optoelectronic and megentic properties (Propiedades mácanicas, optoelectrónicas y magnéticas)

I. INTRODUCTION

Globally, scientists are developing smart materials for a range of potential applications. Halfmetallic materials (HMs) are used to make spintronic devices [1]. The nature of HMs depends on the spin orientation, with one spin channel displaying semiconductor behavior while exhibiting metallic properties [2]. To put it simply, HM is a material in which a band gap is lacking for one kind of spin direction and present for the other kind of spin orientation. Any band gap in the case of a single spin orientation shows that the substance is completely spin-polarized at the Fermi level [3].. The spin-polarized current found in HM ferromagnetic materials may be used as a spin injector, gigantic magnetoresistance, and a building block for magnetic random-access memory [4–6].

Electric and spin current transports are determined by the characteristics of the band structure near the Fermi level in the solids concerned. For the spintronic applications, it would be interesting to examine the extent that the density of states (DOS) near the Fermi level energy (E_F) of the systems considered are spin-polarized. This spin polarization (P^{DOS}) of the DOSs near the E_F is defined as:

$$P^{DOS} = \frac{N\uparrow(E_F) - N\downarrow(E_F)}{N\uparrow(E_F) + N\downarrow(E_F)} \quad (1)$$

Where are the spin-up and spin-down DOSs at the, respectively. This static spin polarization would then vary from −1.0 to 1.0 only. For the half-metallic materials, equals to either −1.0 or 1.0. As mentioned above, the spin polarization defined by Eq. 1 is not necessarily the spin polarization of the transport currents measured in experiments. Indeed, the spin-polarizations measured by using different experimental techniques could differ significantly [7–10]. From the viewpoint of spintronic applications, only the current spin polarization instead of the P^{DOS}, counts.

First, de-Groot et al. reported HM in the Mn-based Heusler

alloys in 1983 [11]. Since the discovery of HM, theoretical research has been done on the half-metallic properties of other materials, including transition metal oxide and dilute magnetic semiconductors [12–16]. There have also been a few experimental experiments conducted [17, 18] Scientists have developed a new class of device that combines conventional microelectronics with spin-dependent phenomena like magnetic sensors and volatile magnetic random-access storage [19] due to the special spin up and spin down capabilities of HM.

The demand for novel nitrides is rising as chemists and material scientists broaden the range of accessible materials. [20, 21] The properties and functionality of materials is essential to sectors such as solar research, ultrasound, fuel cells, and many more are governed by the perovskite structure, which has the fundamental formula ABX_3 where A is a cation, B is a divalent metal ion, and X is a halogen anion (as shown in Figure 1) [22]. However, there are surprisingly few known nitrides with the perovskite structure. Recent computational studies have predicted the stability of rare earth transition metal nitride perovskites [23–26] as well as fascinating ferroic features such ferromagnetism in a variety of $REMN_3$ compounds and ferroelectricity in $LaWN_3$. RE stands for rare earth; M is for W or Re.

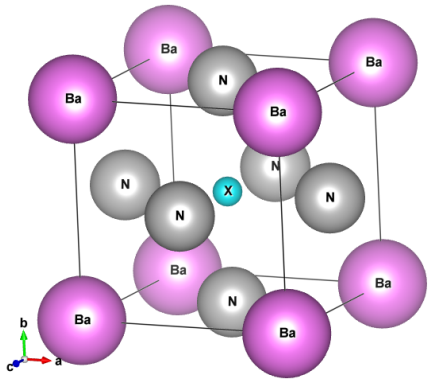

Figure 1. Perovskite crystal structure with $BaXN_3$ (X=K and Rb).

The number of experimental reports is fairly small, and they typically lead to oxynitrides instead, but it has been demonstrated that they also have a number of intriguing characteristics, such as electrochemical activity and enormous magnetoresistance [27, 28]. On the other hand, several anti-perovskites (APs) containing nitrogen have drawn intensive interest because of their attractive physical properties [29].

The inability to synthesize oxygen-free phases in these systems is reflected in the scarcity of nitride perovskites. Further research into nitride perovskites has, however, been made possible by recent work from our team [30] producing thin film perovskite $LaWN_3$ and from Kloβ et al. [31] synthesizing bulk perovskite $LaReN_3$. An oxygen-free, polar rhombohedral perovskite phase called $LaWN_3$ was produced in thin film form and showed a significant piezoelectric response. The use of an activated nitrogen plasma raised the chemical potential of nitrogen, which has been proven to help to stabilize fully produced nitrides [30–37].

Despite a Goldschmidt tolerance factor of 0.99, which would typically indicate cubic symmetry, $LaReN_3$, which demonstrates metallic conductivity and Pauli paramagnetism, was synthesized using high pressure-high temperature techniques and crystallized in triclinic symmetry as a result of orbital ordering distortions [38]. These latest works offer inspiration and possible strategies for increasing the phase space of nitride perovskites [39, 40].

In the present work, the structural, elastic, electronic, magnetic and optical properties of the cubic perovskite $BaXN_3$ (X=K, Rb) are investigated through full potential linearized augmented plane wave method with in Wien2k code [43] To the best of our knowledge, this is the first literature report on the structural, magnetic, electronic, optical and elastic properties of $BaXN_3$ (X=K, Rb) materials.

II. CALCULATION DETAIL

Using density functional theory (DFT) [41,42] as implemented in the full potential linearized augmented plane wave (FP-LAPW) method within the Wien2k package [43], the structural and electronic properties of $BaXN_3$ (X=K, Rb) compounds are investigated. The effects of exchange and correlation were parameterized according to the generalized gradient approximation (GGA-PBE) [44], Also, we have employed the modifed Becke–Johnson (mBJ) [45] scheme for electronic properties' calculation.

Concerning the lattice constants of solids and atomization energies of molecules, the trends observed with the local density approximation (LDA) and the Perdew-Burke-Ernzerhof generalized gradient approximation (GGA-PBE) are the following: LDA clearly underestimates the lattice constants and overestimates the atomization energies. The Perdew-Burke-Ernzerhof generalized gradient approximation (GGA-PBE) which has been generally successful in systems where LDA is lacking and is often taken as a baseline functional for further case-specific corrections.

It's essential to note that local density approximation (LDA) and the Perdew-Burke-Ernzerhof generalized gradient approximation (GGA-PBE) tend to signifcantly underestimate the critical band separation in semiconductors and dielectrics. This limitation stems from their inherent structures, which inadequately account for exchange-correlation energy and its charge derivative. To deal with this issue of band gap underestimation, we adopted the modified Becke-Johnson potential (TB-mBJ), a choice commonly used in recent research. modified Becke-Johnson potential (TB-mBJ) approach is highly recommended for treating the band gap of semi-conducting materials.

The Perdew-Burke-Ernzerhof generalized gradient approximation (GGA-PBE) approximation is first used to get a view of the electronic structures and the

modified Becke-Johnson potential (mBJ-GGA-PBE) method is employed to get a better description of the energy band gaps.

We applied the TB-mBJ functional to account for exchange-correlation effects and improve the calculation of the electronic and optical properties of BaXN3. The TB-mBJ method has been shown to yield accurate band structures for various semiconductors and insulators, as well as to model half-metallic band structures for half-metallic materials [46-49]. One of the key features of the semi-local TB-mBJ exchange potential is the incorporation of a correction factor for the screening effect, improving upon the local approximation of the true potential. Its predictions of bandgaps for a range of materials are as accurate as those produced by the GW method or hybrid functionals. Moreover, compared to standard DFT methods, it is more cost-effective and computationally efficient. A common issue with standard LDA/GGA potentials is the error arising from electron self-interaction and Coulomb repulsion, which tends to underestimate the energy bandgap.

The selected cut-off parameter was $R_{MT}K_{max} = 9$, where R_{MT} is the small atomic radius in the unit cell and K_{max} refers to the size of the largest k vector in the plane wave expansion. In the full-potential scheme, the unit cell of the crystal is partitioned into two different regions: (MT) atomic spheres and (IR) interstitial region. The used energy separation between core and valence states is −6 Ry. The muffin-tin sphere radius (MTS) was equal to 1.97, 1.77, and 1.35 a.u for Ba, X = (K, Rb), and N, respectively. The wave function is extended into two different basic parts. In the atomic sphere, the wave function is extended in atomic-like functions (radial part times spherical harmonics). While in the interstitial region it is expanded in a plane wave basis. Inside the sphere $L_{max} = 10$.

Charge and energy convergence are ensured through a Fourier series expansion of charge density and potential within the interstitial region with a wave vector up to $G_{max} = 14$ (a.u.)$^{-1}$ [50].

The self-consistent field calculation iterations exhibit a convergence criterion of less than 10 − 4 Ry/atom. These adjustments contribute to refining the accuracy and reliability of our computational model, ensuring a comprehensive exploration of the system's electronic structure and properties [51].

A dense mesh of 3000 k-points and the tetrahedral method was utilized.

The mechanical properties are calculated by the analysis of tensor matrix through Chapin method [52] to find the coefficients of nonlinear first order differential equations. For cubic symmetry (C_{11}, C_{12} and C_{44}), they are enough to illustrate mechanical behavior of the studied materials. The optical properties are analyzed through Kramers-Kronig relation [53] between dielectric constants and all the necessary parameters, such as the dielectric function, extinction coefficient and refractive index, which are calculated from the dielectric constants.

III. RESULTS AND DISCUSSION

III.1. Structural properties

According to the literature, many perovskite materials exhibit a cubic structure at room temperature [54], characterized by the highest symmetry with the space group Pm-3m. In the case of the $BaXN_3$ (X=K, Rb) compounds studied, there are two types of atomic positions used to construct the unit cell. In the first scenario, the origin is defined by the cation (Ba or K/Rb), while in the second, the origin is determined by the other cation. Specifically, the K/Rb and Ba atoms are positioned at (0, 0, 0) and (1/2, 1/2, 1/2), respectively. The three nitrogen atoms are located at (1/2, 1/2, 0), (1/2, 0, 1/2), and (0, 1/2, 1/2). Figure 1 illustrates the unit cell of the cubic perovskite structure for the $BaXN_3$ ($X = K$, Rb) compounds.

In order to check the stable magnetic phase, the optimization of this compound was carried out within GGA in its ferromagnetic, non-magnetic, and anti-ferromagnetic configurations. Then, the structural parameters of the equilibrium were calculated by adjusting the total energy as a function of the volume, using Birch Murnaghan equation of state [55]. The total energy-volume of each configuration is shown in Figure 2. According to the obtained results, the ferromagnetic configuration has the lowest energy, which suggests that it is the most stable than the others. We evaluated the equilibrium parameters, the lattice parameter (a), the bulk modulus (B), the derivative of bulk modulus (B′) and the total energy difference between the FM and AFM state ($\Delta E = E_{AFM} - E_{FM}$) of $BaXN_3$ (X=K, Rb) compounds, which are collected in Table 1. From the calculation, it is also found that the FM phase has lower energies than those of the AFM and NM phase, indicating the stability of FM phase ($\Delta E > 0$).

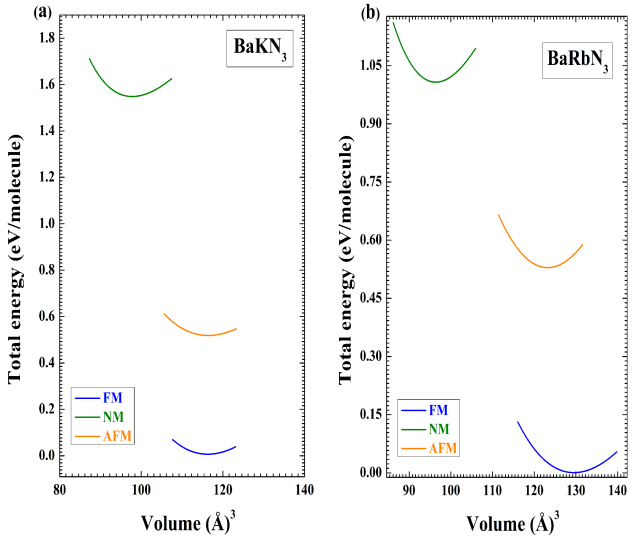

Figure 2. Variation in total energy per unit cell as a function of cell volume for ferromagnetic (FM), anti-ferromagnetic (AFM) and non-magnetic (NM) phases for (a) $BaKN_3$ and (b) $BaKRbN_3$ perovskites, using the GGA-PBE approximation.

Formation energy E_f and cohesive energy E_c are two

important parameters which are used to determine the feasibility of experimental synthesis and required energy to break all bonds associated to the constituent atoms for the compound to decompose into free atoms, respectively. The more negative is E_f, the easier the synthesis. The more negative is E_c, the more stable the structure. To confirm the thermodynamic and chemical stability of the studied perovskite compounds, the cohesive energy E_c can be estimated by using the following formula [56]

$$E_c^{BaXN3} = E_{tot}^{BaXN3} - (E_{Ba} + E_X + 3E_N) \quad (2)$$

where E_{tot}^{BaXN3} is the equilibrium total energy of $BaXN_3$ (X=K, Rb) compounds, and , (X=K, Rb) and are the total energies of the isolated atoms. To define the formation energy, we use the following equation [57]:

$$E_f^{BaXN3} = E_{tot}^{BaXN3} - (E_{Ba}^{bulk} + E_X^{bulk} + 3E_N^{bulk}) \quad (3)$$

Here, E_{tot}^{BaXN3} is the total energy of $BaXN_3$ E_{Ba}^{bulk}, E_X^{bulk} and $3E_N^{bulk}$ (X=K, Rb) are the total energies for each Ba, (X=K, Rb) and N atoms in their bulk states.

Furthermore, the Table 1 includes the energy of formation and cohesive energy for our compounds, offering valuable insights into their stability and bonding characteristics.

The energy of formation represents the energy change accompanying the formation of a compound from its constituent elements, providing information about the compound's thermodynamic stability. On the other hand, cohesive energy measures the energy required to separate the atoms within a compound into isolated atoms, refecting the strength of chemical bonds and interatomic interactions. These parameters are essential for predicting material stability, chemical reactivity, and potential applications in various felds, including catalysis, materials science, and solid-state chemistry. The negative value of formation energy shows the thermodynamical stability of $BaXN_3$ (X=K, Rb).

III.2. Elastic properties

To investigate the elastic properties, we use IRelast package integrated in the WIEN2k. The study of the elastic properties informs on the behavior of this compound regarding ductility, brittleness and application of the external forces.

For cubic symmetry crystals, three independent elastic constants C_{11}, C_{12} and C_{44} are used to determine the mechanical properties, such as the rigidity and stability of the material under study. The calculated values of elastic constants C_{ij} are presented in Table 2. The bulk modulus B can be calculated from elastic constants using the relation

$$B = \frac{c_{11} + 2C_{12}}{3} \quad (4)$$

All the elastic constants are positive and satisfy the criteria $C_{11} > 0$; $C_{44} > 0$; (C_{11}-C_{12})¿0; (C_{11}+2C_{44})>0; $C_{12} < B < C_{11}$ for mechanical stability [58]. Table 2 presents the results of anisotropy factor A, Young's modulus E, Poisson's ratio ν and Pugh's index ratio B/G by using the following relations [59–66].

$$A = \frac{2C_{44}}{C_{11} - C_{12}} \quad (5)$$

$$E = \frac{9BG}{3G + B} \quad (6)$$

$$\nu = \frac{3B - 2G}{2(3B + G)} \quad (7)$$

$$G = \frac{G_R + G_V}{2} \quad (8)$$

$$G_R = \frac{5(C_{11} - C_{12})C_{44}}{4C_{44} + 3(C_{11} - C_{12})} \quad (9)$$

$$G_V = \frac{C_{11} - C_{12} + 3C_{44}}{5} \quad (10)$$

The classification of a material as a ductile or brittle can be made on the basis of the B/G ratio [67]. If this ratio is smaller than 1.75, the material shows brittle nature. Otherwise it shows ductile character. On the basis of Pugh's criteria [68] all the compounds show ductile nature. Ductility or brittleness of compounds can also be inferred from the poison's ratio γ [69].

The material is ductile if the γ is greater than 0.26, otherwise it is brittle. The values listed in Table 2 confirmed that all compounds show ductile behavior. The elastic anisotropy factor A for all studied compounds is also presented in Table 2. For isotropic materials, this factor is equal to 1, and deviation of values from 1 represents a measure of the anisotropy possessed by the material. The values for $BaKN_3$ and $BaRbN_3$ are 1.07 and 0.15, respectively. These results clearly reveal that all compounds are anisotropic.

III.3. Electronic and magnetic properties

Figure 3 show how the spin-polarized band structures for $BaKN_3$ and $BaRbN_3$ compounds at the equilibrium lattice constant within Perdew-Burke-Ernzerhof generalized gradient approximation (GGA-PBE) and improved the modified Beck Johnson TB-mBJ approximations. These are drawn along the high symmetry k-path in the first Brillouin zone. We can see, for the spin-down states (Figure 3 (b, d)) of $BaKN_3$ and $BaRbN_3$ compounds, a metallic nature due to the intersecting of the valence band with Fermi level. In the other hand, for the spin-up channel (Figure 3 (a, c)), the compound shows an insulating character. In this channel (spin-up), we can see that $BaKN_3$ and $BaRbN_3$ compounds have an indirect band gap from Γ to M, the values of the band gap of $BaKN_3$ and $BaRbN_3$ are 2.79, 4.29 eV in GGA-PBE and 5.75, 6.27 eV in mBJ-GGA-PBE respectively which are very large. The half-metallic gap (HMGap) is deduced from the valence band maximum (VBM) which is nearer than the conduction band minimum (CBM) to Fermi level, for both approaches (GGA and TB-mBJ). The values of HM gap are

1.27, 2.74 eV for $BaKN_3$ and 3.17, 3.69 eV for $BaRbN_3$ in GGA-PBE and mBJ-GGA-PBE respectively. Therefore, we can see that the TB-mBJ method opens the band gap, located at Γ and M high symmetry points, for conduction band minimum (CBM) and valence band maximum (VBM), respectively. To explain the contribution of the various electronic states of band structures, it is also interesting to determine the total and partial densities of states, TDOS and PDOS, respectively.

As given in Figure 4, the TDOS and PDOS using GGA-PBE and mBJ-GGA-PBE are plotted for both majority (up) and minority (down) spin channels, respectively. Indeed, the density of states (DOS) reveals that p states of N atoms mainly contribute to the TDOS for the spin-up and -down channel states around the Fermi level. However, p states of K and Rb have a little contribution to the spin-down channel states. Moreover, p states of Ba have no contribution.

Figures 3, clearly shows that in the spin-down state, no band-gap is present, while in the spin-up state, a semiconducting bandgap appears. This indicates that the reported perovskite compounds exhibit half-metallic behavior. Our analysis of the electronic properties of $BaKN_3$ and $BaRbN_3$ suggests that these alloys could be promising candidates for spintronic applications, owing to their semiconducting nature in one spin channel.

The integer spin of magnetic moments plays a role in determining the nature of the electronic states in half metals, influencing their magnetic and electrical properties. It's worth noting that materials with half metallic property should possess integer spin magnetic moment or close to integral values. In addition, the spin magnetic moment depends on other factors such as crystal structure, electronic configuration, and interactions also play a role [70]. Our perovskites $BaKN_3$ and $BaRbN_3$ also possess integer spin magnetic moments which are presented in Table 3. From this table, we can understand that the perovskites $BaKN_3$ and $BaRbN_3$ have integer magnetic moments of 6 μB. Therefore, they exhibit HM behavior.

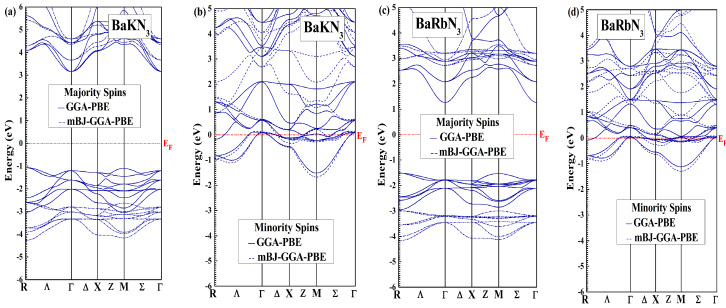

Figure 3. Comparison of GGA-PBE and mBJ-GGA-PBE spin-polarized band structures spin up, and spin down of $BaKN_3$ (a, b) and $BaRbN_3$ (c, d) calculated at the equilibrium lattice constant. The horizontal dashed line indicates the Fermi level

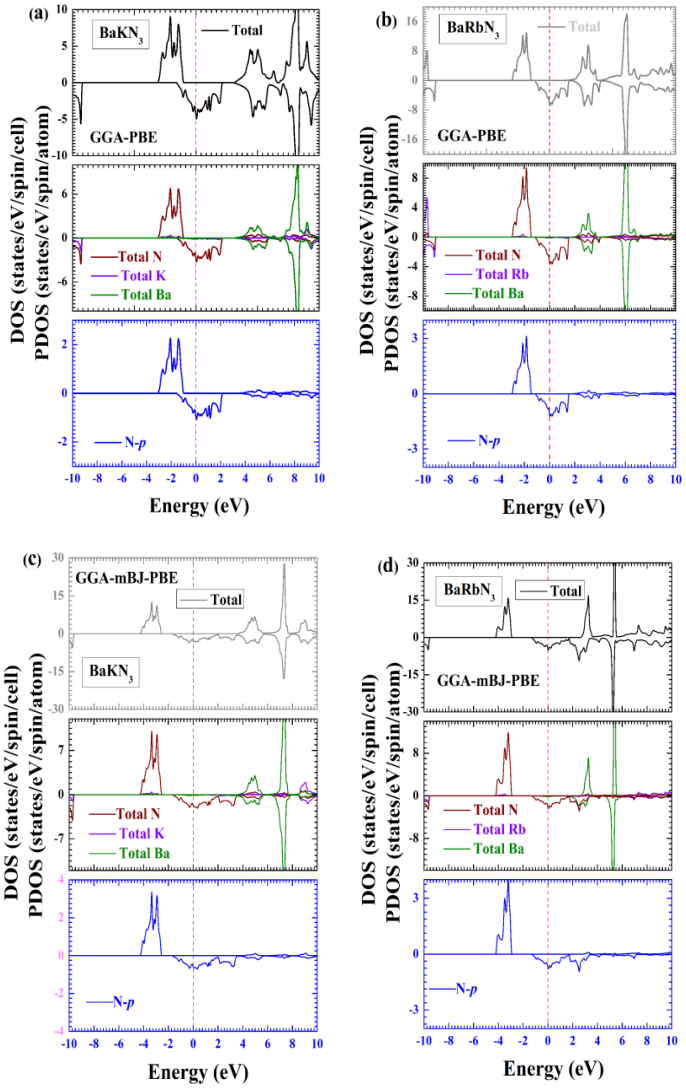

Figure 4. Spin-dependent total and partial densities of states for $BaKN_3$ (a,c) and $BaRbN_3$ (b, d) using GGA-PBE and mBJ-GGA-PBE. The vertical dashed line indicates the Fermi level. Positive and negative values of DOS hold for spin-up and spin-down states, respectively.

We remark that the interstitial and N magnetic moments are the highest, whereas that of K and Rb are the lowest. Despite TB-mBJ results show a slight increase in the magnetic moment of N atom.

III.4. Optical Properties

The theoretical equilibrium lattice constants are used to explore all optical characteristics. The optical properties of perovskite $BaXN_3$ (X=K, Rb) material were studied using the dielectric function $\epsilon(w)$ that describes the system response to an external electromagnetic field t hrough t he i nteraction of photons with electrons [71]:

III.4.1. Dielectric function (The real and imaginary part)

The real dielectric constant is a measure of the polarization of the material. The imaginary dielectric constant is a measure of the dielectric losses. The ratio of complex to real dielectric

constant is the loss of tangent of the dielectric material. The $\epsilon(w)$ is made up of two parts: the real and imaginary components, which are written as $\epsilon(w) = \epsilon_1(w) + i\epsilon_2(w)$ [72].

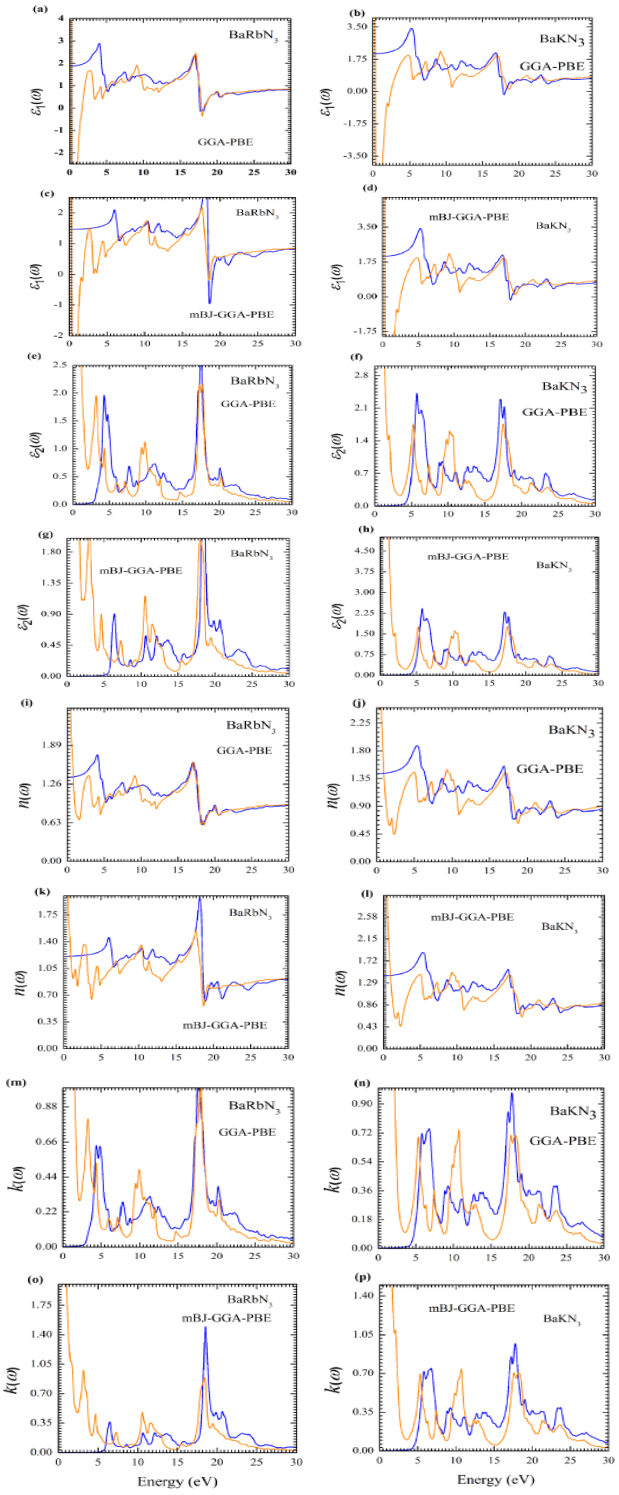

Figure 5. Calculated spin up (in blue) and down (in orange) of $BaXN_3$ (X=K, Rb), (a-d) real part of the dielectric function $\epsilon_1(w)$, (e-h) imaginary part of the dielectric function $\epsilon_2(w)$, (i-l) refractive index $n(w)$ and (m- p) extinction co-efficient $\kappa(w)$ as a function of photon energy for $BaKN_3$ and $BaRbN_3$ with GGA-PBE and mBJ-GGA-PBE, as indicated.

Figure 5 (a-d) show the computed $\epsilon_1(w)$ for both materials using GGA-PBE and mBJ-GGA-PBE, while the imaginary part of the $\epsilon_2(w)$ (dielectric function) is shown in Figure 5 (e-h) within the input photon energy range of up to 30 eV, $\epsilon_1(w)$ characterizes photon dispersion within the material, whereas the imaginary part $\epsilon_2(w)$ is directly associated with the electronic band structure, representing the absorption of light in the crystal. For both materials, the estimated static dielectric function $\epsilon_1(0)$ is presented in Figure 5 (a-d), where $\epsilon_1(0)$ = 3.39, 3.44 for $BaKN_3$ and 2.89, 2.07 for $BaRbN_3$ in GGA-PBE and mBJ-GGA-PBE respectively, indicating that $BaKN_3$ dissipates more energy than $BaRbN_3$. According to the Penn model [73], materials with greater $\epsilon_1(0)$ (static dielectric functions) have smaller band gap energy, while those with lower values have larger band gap energy.

According to the calculations, these materials follow the Penn model. The Figure 5 (a-d) show that when photon energy is low, both materials waste more energy, and when photon energy is high, the behavior is the same.

$\epsilon_2(w)$ is shown in Figure 5 (e-h), which shows the polarizability of a material. Both materials have no polarization at 0 eV energy of an incident photon, as seen in the figures. It should be stated that for the interpretation of a structure (peak) in the optical spectra of the systems, it does not seem realistic to give a single transition assignment resembling the energy of the peak since numerous transitions between the occupied and the unoccupied energy bands for a particular structure can be satisfied [74]. The imaginary part shows that there exists an optical gap for the spin-up channel for our compounds, which supports our previous observation that the spin-up channel shows semiconducting character.

III.4.2. Refractive index $n(w)$ and the extinction coefficient $\kappa(w)$

Refractive index $n(w)$ is an important optical parameter to study the potential applications of a material in the field of optical and photonic devices [75]. The expression for refractive index is:

$$n(w) = \frac{((\epsilon_1{}^2(w) + \epsilon_2{}^2(w))^{1/2} + \epsilon_1(w))^{1/2}}{\sqrt{2}} \tag{11}$$

$$\kappa(w) = \frac{((\epsilon_1{}^2(w) + \epsilon_2{}^2(w))^{1/2} - \epsilon_1(w))^{1/2}}{\sqrt{2}} \tag{12}$$

where, n is the real part of the complex refractive index (refractive index) and κ is the imaginary part of the refractive index (extinction coefficient).

The spectra of refractive index $n(w)$ for $BaKN_3$ and $BaRbN_3$ are shown in Figure 5 (i-l). We can conclude from the plots that both curves are comparable with those of the real part of the dielectric function. The zero-frequency $n(0)$ refractive index is found 1.45, 1.43 for $BaKN_3$ and 1.37, 1.22 for $BaRbN_3$ in GGA-PBE and mBJ-GGA-PBE, respectively. Beyond the zero-frequency, the curve reached to peak value of 1.88 at 5.33 eV, 1.88 at 5.38 eV for $BaKN_3$ and 1.73 at 4.06 eV, 1.95 at 18.16

eV for $BaRbN_3$ in GGA-PBE and mBJ-GGA-PBE respectively. Since the value becomes greater than unity, this shows that photons slow down after interacting with the electron of a material. The $n(w)$ is a useful statistic property for estimating light refraction, particularly in photoelectric applications.

As photon energy increases, it is observed that the refractive index decreases towards zero and stabilizes at values close to zero. In contrast, a distinct peak in the refractive index is prominent in the infrared region. The high value of the refractive index indicates that, during light transmission, incident photons interact with more valence electrons, leading to high polarization and consequently a reduction in the speed of light [76–78]. In summary, the graphical representation underscores the dynamic behavior of refractive index and extinction coefficient with changing photon energy, elucidating the material's optical response and its impact on light transmission characteristics.

The extinction coefficient $\kappa(w)$, as shown in Figure 5 (m-p), closely follows the behavior of $\epsilon_2(w)$. The variation of $k(w)$ from $\epsilon_2(w)$ is attributed to small optical conductivity [79]. The extinction coefficient $k(w)$ may constitute an important criterion for the phenomenon of fluorescence; the higher the value of k, the higher the fluorescence [80].

For the extinction coefficient $k(w)$, the values reach maximum at about 17.75 and 18.54 eV and indicate strongest absorption at the edge and above 4.12 and 5.52 eV for $BaKN_3$ and $BaRbN_3$ respectively within mBJ-GGA-PBE. It is clear that the maximum value of $k(w)$ of $BaRbN_3$ is higher than that of the $BaKN_3$ compound, indicating that $BaRbN_3$ exhibits a much stronger ultraviolet absorption compared to that of the $BaKN_3$. On the other hand, the extinction coefficient $k(w)$ may constitute an important criterion for the phenomenon of fluorescence. Hence, according to this characteristic, $BaRbN_3$ should be more fluorescent in the ultraviolet range. At low frequency (energy) in the infrared–visible region, the extinction coefficient is zero for both compounds, indicating that $BaXN_3$ (X=K, Rb) are effectively transparent.

IV. SUMMARY AND CONCLUSION

The structural, electronic, magnetic, optical and elastic properties of nitride-based perovskites $BaXN_3$ (X = K, Rb) are studied using density functional theory (DFT). The structural study reveals that both compounds have stable and cubic structure. The calculated total energies show that the total energy difference $\Delta E = E_{AFM} - E_{FM}$ are positive, thus; the compounds $BaXN_3$ are structurally stable in the ferromagnetic state. The negative value of formation energy shows the thermodynamical stability of $BaXN_3$ (X=K, Rb). The GGA-PBE approximation is first used to get a view of the electronic structures and the mBJ-GGA-PBE potential methods are employed to get a better description of the energy band gaps. The magnetic moment of the of BaXN3 compounds is 6 μB, which originates mainly from the N-p states.

Electronic properties were analyzed in two ways, i.e. by DOS and band structures with the GGA-PBE and mBJ-GGA-PBE, one can see that for BaXN3 in both GGA-PBE and mBJ-GGA-PBE there is an energy gap around the Fermi level in the majority-spin (spin-up) channel while the minority-spin (spin-down) channel is strongly metallic, that is to say, it exhibits a true HM characteristic with 100 % spin-polarization around the Fermi level.

The GGA-PBE approximation is first used to get a view of the electronic structures and the mBJ-GGA-PBE potential methods are employed to get a better description of the energy band gaps. The mechanical characteristics of $BaXN_3$ (X=K, Rb) compounds show that the compounds of interest are anisotropic, ductile, scratch-resistant, and elastically stable. The optical properties are investigated within the energy ranges of 0 eV-30 eV of incident photon energies. From the analyses, the main peak in the imaginary part of the spin-up channel corresponds to the transitions between the valence band (VB) and the conduction band (CB). Therefore, our compounds are identified as potential candidates for spintronic applications and high-performance electronic devices, which are of high technological importance due to their possible half-metallic character.

REFERENCES

[1] I. Zutic, J. Fabian and S. D. Sarma, Rev. Mod. Phys. 76 (2004) 323

[2] S. A. Wolf, D. D. Awschalom, R. A. Buhrman, J. M. Daughton, V. S. von Molnár., M. L Roukes and D. M. Treger, Science. **294** (2001) 1488.

[3] K. L. Wang, J. G. Alzate and P. Khalili Amiri, J. Phys. D: Appl. Phys. **46** (2013) 074003-074012.

[4] H. Lee, F. Ebrahimi, P. K. Amiri and K. L. Wang, IEEE Magn. Lett. 7 (2016) 1.

[5] W. Zhao, E. Belhaire, C. Chappert, P. Mazoyer, IEEE. Computer. Society. Annual. Symposium on VLSIIEEE. 40 (2008) 40.

[6] K. Nikolaev, P. Kolbo, T. Pokhil, X. Peng, Y. Chen, T. Ambrose and O. Mryasov, Appl. Phys. Lett. **94** (2009) 222501.

[7] R. J. Soulen Jr, J. M. Byers, M. S. Osofsky, B. Nadgorny, T. Ambrose, S. F. Cheng, P. R. Broussard, C. T. Tanaka, J. Nowak, J. S. Moodera, A. Barry and J. M. D. Coey, Science 282 (1998) 85.

[8] J. M. De Teresa, A. Barthélémy, A. Fert, J. P. Contour, F. Montaigne and P. Seneor, Science 286 (1999) 507.

[9] P. A. Dowben, N. Wu and C. Binek, J. Phys.:Condens. Matter 23 (2011)171001.

[10] X. Kozina, J. Karel, S. Ouardi, S. Chadov, G. H. Fecher and C. Felser, G. Stryganyuk, B. Balke, T. Ishikawa, T. Uemura, M. Yamamoto, and E. Ikenaga, Phys. Rev. B 89 (2014) 125116.

[11] S. Tsunegi,Y. Sakuraba, M. Oogane, K. Takanashi and Y. Ando, Appl. Phys. Lett. 93 (2008) 112506.

[12] T. Ishikawa, T. Marukame, H. Kijima, K. I. Matsuda, T. Uemura, M. Arita and M. Yamamoto, Appl. Phys. Lett. 89 (2006) 192505.

[13] Y. Wang, J. Zheng*,Z. Ni, R. Fei, Q. Liu, R. Quhe, C. Xu, J. Zhou, J. Gao and J. Lu, Nano. 07 (2012) 1250037.

[14] H. X. Liu, H.Y. Honda, T. Taira, K. I. Matsuda, M Arita, T. Uemura and M. Yamamoto, Appl. Phys. Lett. 101 (2012) 132418.
[15] J. Y. T. Wei, N. C. Yeh, R. P. Vasquez and A. Gupta, J. Appl. Phys. 83 (1998) 7366.
[16] M. Ram, A. Saxena, A. E. Aly and A. Shankar, RSC Adv. 10 (2020) 7661
[17] J. H. Park, S. K. Kwon and B. I. Min, Phys. Rev. B: Condens. Matter Mater. Phys. 65, (2002) 174401.
[18] I. Galanakis and E. Şaıoğlu, Appl. Phys. Lett. **99** (2011) 052509.
[19] Z. Wang, Q. Jing, M. Zhang, X. Dong, S. Pan and Z. Yang, RSC Adv. 4 (2014) 54194.
[20] W. Sun, C. J. Bartel, E. Arca, S. R. Bauers, B. Matthews, B. Orvañanos, B. R. Chen, M. F. Toney, L. T. Schelhas, W. Tumas, J. Tate, A. Zakutayev, S. Lany, A. M. Holder and G. Ceder, Nat. Mater. **18** (2019) 732.
[21] A. Zakutayev, S. R. Bauers and S. Lany, Chem. Mater. **34** (2022) 1418.
[22] N. Hasan, M. Arifuzzaman and A. Kabir, RSC Adv. **12** (2022) 7961.
[23] S. F. Matar and G. Demazeau, J. Solid State Chem. **183** (2010) 994.
[24] R. Sarmiento-Pérez, T. F. T. Cerqueira, S. Körbel, S. Botti and M. A. L. Marques, Chem. Mater. **27** (2015) 5957.
[25] M. C. Jung, K. W. Lee and W. E. Pickett, Phys. Rev. B. **97** (2018) 121104.
[26] V. A. Ha, H. Lee and F. Giustino, Chem. Mater. **34** (2022) 2107.
[27] Y. W. Fang, C. A. J. Fisher, A. Kuwabara, X. W. Shen, T. Ogawa, H. Moriwake, R. Huang and C. G. Duan, Phys. Rev. B. **95** (2017) 014111.
[28] J. A. Flores-Livas, R. Sarmiento-Pérez, S. Botti, S. Goedecker and M. A. L. Marques, J. Phys. Mater. **2** (2019) 025003.
[29] Y. Wang, Q. Wang, Z. Liu, Z. Zhou, S. Li, J. Zhu, R. Zou, Y. Wang, J. Lin and Y. Zhao, J. Power. Sources. **293** (2015) 735.
[30] P. Bacher, P. Antoine, R. Marchand, P. L'Haridon, Y. Laurent and G. Roult, J. Solid State Chem. **77** (1988) 67.
[31] N. E. Brese and F. DiSalvo, J. Solid State Chem. **120** (1995) 378.
[32] S. J. Clarke, B. P. Guinot, C. W. Michie, M. J. Calmont and M.J. Rosseinsky, Chem. Mater. **14** (2002) 288.
[33] M. Yang, J. Oró-Solé, A. Kusmartseva, A. Fuertes and J. P. Attfield, J. Am. Chem. Soc. **132** (2010) 4822.
[34] A. Fuertes, J. Mater. Chem. **22** (2012) 3293.
[35] A. P. Black, H. E. Johnston, J. Oró-Solé, B. Bozzo, C. Ritter and C. Frontera, Chem. Commun. **52** (2016) 4317.
[36] K. R. Talley, J. Mangum, C. L. Perkins, R. Woods-Robinson, A. Mehta, B. Gorman, G. L. Brennecka and A. Zakutayev, Adv. Electron. Mater. **5** (2019) 1900214.
[37] R. Niewa, Eur. J. Inorg. Chem. 2019 (2019) 3647.
[38] K. R. Talley, C. L. Perkins, D. R. Diercks, G. L. Brennecka and A. Zakutayev, Scienc.e **374** (2021) 1488.
[39] S. D. Kloß, M. L. Weidemann, J. P. Attfield and J. P. Angew. Chem., Int. Ed. **60** (2021) 22260.
[40] V. N. Antonov, L. V. Bekenov and A. Ernst, Phys. Rev. B. 94 (2016) 035122
[41] P. Hohenberg and W. Kohn, Phys. Rev. 136 (1964) B864
[42] W. Kohn and L. J. Sham, Phys. Rev. 140 (1965) A1133
[43] P. Blaha, K. Schwarz, G. K. H. Madsen, D. Kvasnicka and J. Luitz, WIEN2k, An Augmented Plane Wave Plus Local Orbitals Program for Calculating Crystal Properties (Vienna University of Technology, Austria, 2012).
[44] J. P. Perdew, K. Burke and M. Ernzerhof, Phys. Rev. Lett. 77 (1996) 3865
[45] F. Tran and P. Blaha, Phys. Rev. Lett. 102 (2009) 226401
[46] D. Koller, F. Tran and P. Blaha, Phys. Rev. B 83 (2011) 195134.
[47] J.P. Perdew, K. Burke and M. Ernzerhof, Phys. Rev. Lett. 77 (1996) 3865
[48] D.J. Singh, Phys. Rev. B 82 (2010) 155145
[49] S.D. Guo and B.G. Liu, Europhys. Lett.93 (2011) 47006
[50] Y. Rakita, S. R. Cohen, N. K. Kedem and G. Hodes, MRS Commun. 5 (2015) 623
[51] F. Wooten, Optical Properties of Solids. Academic Press, New York (1972).
[52] G. Grimvall, Thermophysical Properties of Materials. Amsterdam: Elsevier (1999).
[53] R. Hill, The Elastic Behaviour of a Crystalline Aggregate. Proc. Phys. Soc. Sect. A. 65 (1952) 349
[54] J. Bartolome, D. Gonzalez, R. Navarro, C. Ridou, M. Rousseau and A. Bulou, J. Phys. C. Solid State Phys. 20 1987) 2819.
[55] F.D. Murnaghan, Proc. Natl. Acad. Sci. U.S.A. 30 (1944) 244
[56] H. Benaissa, S. Benatmane, S. Amari, K. Obodo, L. Beldi, H. Bendaoud, and B. Bouhafs, Spin 8 (2018) 1850017.
[57] S. Benatmane, H. Bendaoud, L. Beldi, B. Bouhafs, S. Méçabih, and B. Abbar, J. Supercond. Nov. Magn., 31 (2018) 2767.
[58] M. Born, Proc. Camb. Phil. Soc. 36 (1940) 160
[59] W. Voigt, Lehrbuch der Kristallphysik, Taubner, Leipzig, 1928.
[60] A. Reuss and Z. Angew, Math. Mech. 9 (1929) 49
[61] R. Hill, The elastic behaviour of a crystalline aggregate, Proc. Phys. Soc. 65 (1952) 349
[62] S.F. Pugh, Philos. Mag. A 45 (1954) 823.
[63] R. Gaillac, P. Pullumbi and F.X. Coudert, J. Phys. Condens. Matter. 28 (2016) 275201.
[64] V. Erofeev and I. Pavlov, J. Appl. Mech. Tech. Phys. 56 (2015) 1015.
[65] F. Tanaka and H. Takahashi, J. Chem. Phys. 83 (1985) 6017.
[66] Z. Wu, E. Zhao, H. Xiang, X. Hao, X. Liu and J. Meng, Phys. Rev. B. 76 (2007) 054115
[67] F. Peng, L. Han, H. Fu and X. Cheng, Phys. Status. Solidi. 246 (2009) 1590.
[68] N. Korozlu, K. Colakoglu, E. Deligoz and S. Aydin, J. Alloy. Comp. 546 (2013) 157.
[69] G. Chen and P. Zhang, Defence. Tech. 9 (2013) 131.
[70] S. Benatmane and B. Bouhafs, Comput. Condens. Matter, 19 (2019) e00371

[71] S. Benatmane and S. Cherid, JETP Letters, 111 (2020) 694–702.
[72] S. Benatmane, M. Affane, Y. Bouali, B. Bouadjemi, S. Cherid, and W. Benstaali, Rev. Mex. Fis. 69 (2023) 011003
[73] S. Benatmane, L. Beldi, H. Bendaoud, S. Méçabih, B. Abbar, and B. Bouhafs, Ind. J. Phys. 93 (2019) 627
[74] G. Harbeke, In Optical properties of Solids: F. Abelès (Ed.), North-Holland, Amsterdam, 1972.
[75] P. J. L. Hervé and L. K. J. Vandamme, Infrared Phys. Technol. 35 (1994) 609.
[76] B. Bouadjemi, M. Houari, S. Benatmane, M. Matougui, S. Haid, S. Bentata, and B. Bouhafs, Comput. Condens. Matter. 26 (2021) e00531
[77] M. Fox, Optical properties of solids. Oxford master series in condensed matter physics,.ed: Oxford University Press, Oxford, (2001).
[78] S. Benatmane, Emerg. Mater.5 (2021) 1797
[79] S. Azam, S. Goumri-Said, S. A. Khan and M B. Kanoun, J. Phys. Chem. Solid. 138 (2020) 109229
[80] S.Z.A. Shah, S. Niaz, T. Nasir and J. Sifuna, Results. Chem. 5 (2023) 100828.

Table 1. Calculated equilibrium lattice parameter (a), bulk modulus (B), derivative of bulk modulus (B'), the cohesive energy E_c (eV), formation energy E_f (eV) and the energy difference $\Delta E = E_{AFM} - E_{FM}$ (eV) for the ferromagnetic (FM), anti-ferromagnetic (AFM) and non-magnetic (NM) states for the three types of $BaXN_3$ (X=K, Rb) perovskites by the GGA-PBE.

Compound	Method		a	B	B'	E_c	E_f	ΔE
			(Å)	(GPa)		(Ry)	(Ry)	(meV)
$BaKN_3$	GGA-PBE	FM	4.88	28	3.50	-1.42	-0.28	
		AFM	4.77	25	4.89	-1.39	-0.25	
		NM	4.60	34	7.23	-1.31	-0.17	467.02
$BaRbN_3$	GGA-PBE	FM	5.06	38	4.53	-1.36	-0.23	
		AFM	5.00	35	3.83	-1.32	-0.19	
		NM	4.58	36	5.50	-1.29	-0.16	593.45

Table 2. Calculated elastic constants C_{ij} (GPa), bulk modulus B (GPa), shear modulus G (GPa), Young's modulus E (GPa), Poisson's ratio ν, anisotropy factor A and Pugh's ratio B/G for the $BaXN_3$ (X=K, Rb) perovskites.

	C_{11}	C_{12}	C_{44}	B	GV	GR	G	B/G	A	E	ν
$BaKN_3$	48.22	17.98	16.32	28.06	15.84	15.81	15.82	1.77	1.07	39.95	0.36
$BaRbN_3$	95.01	10.33	6.76	38.56	20.99	10.19	15.59	2.47	0.15	41.22	0.32

Table 3. Calculated total, partial and interstitial magnetic moments, half-metallic gaps (HM) (eV) and energy gaps E_g (eV) of the the $BaXN_3$ (X=K, Rb) perovskites compounds by the GGA-PBE and mBJ-GGA-PBE.

	Methods	μ_{inters}	μ_{Ba}	μ_X (X=K, Rb)	μ_N	μ_{tot}	HM gap	E_g	Band gap type
		(μB)	(μB)	(μB)	(μB)	(μB)	(eV)	(eV)	
$BaKN_3$	GGA-PBE	0.51	-0.01	0.16	1.77	6.00	1.27	2.79	indirect (Γ-M)
	mBJ-GGA-PBE	-0.05	-0.04	0.12	1.99	6.00	2.74	5.75	
$BaRbN_3$	GGA-PBE	1.07	-0.02	0.08	1.62	6.00	3.17	4.29	indirect (Γ-M)
	mBJ-GGA-PBE	0.28	-0.04	0.06	1.90	6.00	3.69	6.27	